Available online at www.sciencedirect.com
ScienceDirect
Journal of Applied Geophysics 60 (2006) 100–114
JOURNAL OF APPLIED GEOPHYSICS
www.elsevier.com/locate/jappgeo

Investigation of a slope endangered by rainfall-induced landslides using 3D resistivity tomography and geotechnical testing

S. Friedel [a,b,*], A Thielen [a,1], S.M. Springman [a,1]

[a] *Institute for Geotechnical Engineering, Eidgenössische Technische Hochschule Zürich (ETHZ), 8093 Hönggerberg, Switzerland*
[b] *Femlab GmbH, Technoparkstr. 1, 8005 Zürich, Switzerland*

Received 30 April 2005; accepted 6 January 2006

Abstract

Rainfall-induced landslides pose a common problem in areas with slopes steeper than the friction angle of the soil. A series of such landslides in North Switzerland inspired a detailed geophysical and geotechnical site investigation prior to a monitoring experiment.

High-resolution 2D and 3D electrical resistivity tomography (ERT) was used to derive a detailed subsurface image, which was verified by direct penetration tests, boreholes and laboratory analysis of soil samples with respect to grain size distribution and plasticity. Resolution analysis of ERT configurations proved a combination of Wenner–, Schlumberger– and Dipole–Dipole data to be a reasonable compromise between measurement time and model accuracy. Furthermore, a statistical approach to reducing subjectivity in the interpretation of 3D resistivity models is suggested. Applying this classification scheme to field data yields a model in very good agreement with the geotechnical model. The 3D resistivity model is then interpreted quantitatively using laboratory data and a constitutive relation accounting for clay and silt contents. The dominant influence of saturation on resistivity predicted by this model is confirmed and exemplified during repeated surveys in a dry and a wet period. In wet summer 2004, a silty sand layer of high water saturation is confined between two less permeable layers, the sandstone bedrock below and a clayey sand layer on top. This layer may locally form an aquifer, which becomes rapidly saturated during heavy rainfalls and contributes to the risk of failure. The combined ERT and geotechnical survey helped to optimize the design of the forthcoming monitoring experiment and may be used as a guideline for the investigation of similar slope conditions.

Keywords: Electrical resistivity; Tomography; Slope stability; Rainfall-induced landslides

1. Introduction

Rainfall-induced landslides are a common problem in areas with slope angles steeper than the friction angle of the soil. Such slopes are only stable within a certain range of water saturation, when the effect of suction creates an apparent cohesion between the soil particles and enhances the shear resistance (e.g., Fredlund and Rahardjo, 1993; Springman et al., 2003). Suction and

* Corresponding author. Fax: +41 44 445 2141.
Email addresses: sven.friedel@igt.baug.ethz.ch (S. Friedel), andrea.thielen@igt.baug.ethz.ch (A. Thielen), sarah.springman@igt.baug.ethz.ch (S.M. Springman).
[1] Fax: +41 1 633 10 79.

0926-9851/$ - see front matter © 2006 Elsevier B.V. All rights reserved.
doi:10.1016/j.jappgeo.2006.01.001

shear resistance are reduced significantly if the saturation is above a critical value. Especially after heavy rainfalls, water saturation may exceed a critical limit in certain parts of the slope, initiating local failure leading to a landslide or debris flow.

A series of 42 landslides occurred in May 2002 in North Switzerland near the river Rhine after an extreme event, in which 100 mm rain fell in 40 min (Fischer et al., 2003). An area especially affected was located near the municipalities of Freienstein–Teufen, Rüdlingen, and Buchberg where the river Toess flows into a sharp bend of the Rhine (Fig. 1). In this area, known as Toessegg, an experimental test site was planned in order to study the interrelation of the many factors influencing the creation of landslides, e.g., rainfall, infiltration, saturation, suction and vegetation. For this purpose, it was planned to install a monitoring system for a period of 1 year, recording data for a variety of sensors such as a rain gauge, tensiometers, TDR probes, flushing piezometers and MoisturePoint devices (Thielen and Springman, 2005; Thielen et al., 2005).

In this paper, we report the results of a detailed geophysical and geotechnical site investigation prior to the installation of these sensors. The aim of the study was to derive a detailed image of the subsurface regarding the sequence of layers and the depth of the bedrock interface, in order to choose an optimum position of the sensors and later to provide constraints to the interpretation of the monitoring data. As geotechnical testing methods (e.g., dynamic penetration tests, boreholes and sampling) are known to be invasive and may disturb the near-surface hydraulic regime, emphasis was placed on non-invasive and high-resolution methods such as Electrical Resistivity Tomography (ERT) and Ground Penetrating Radar (GPR).

Geophysics have been used for many years to investigate landslides, mainly after their development as an aid to back-analysis (see overview articles by Bogoslovsky and Ogilvy, 1977; McCann and Forster, 1990; Frappa and Lebourg, 2001). Geophysical methods applied to slope stability analysis have been reviewed by Hack (2000). In particular, geoelectrical and electromagnetic methods have recently been used most intensively to investigate soil and groundwater conditions of landslide areas (Schmutz et al., 2000; Godio and Bottino, 2001). High-resolution 2D geoelectrical tomography has been used successfully applied to map slipped masses (Lapenna et al., 2003) and, including permanently installed borehole electrodes, to monitor

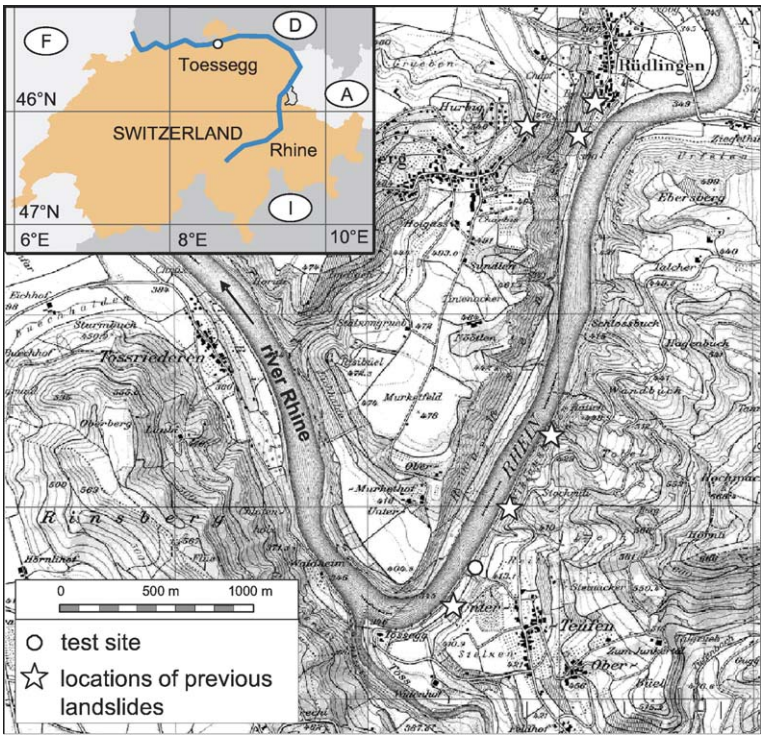

Fig. 1. Location of the test site near Toessegg in North Switzerland. The steep banks near the sharp bend of river Rhine were subject to several landslides in May 2002 (star marks).

saturation changes on a landslide endangered site after heavy rainfalls (Suzuki and Higashi, 2001).

Based on the experiences of these state-of-the art surveys, but using the increased capabilities of modern field equipment and inversion codes, in this study we present a comprehensive 3D subsurface model by using several parallel and crossed geoelectrical survey lines with up to 100 electrodes. The model is verified by data from a detailed geotechnical survey including dynamic penetration tests, drilling and sample analysis with respect to grain size distribution and plasticity. Because the ERT and geotechnical models agreed very well, we present a statistical approach to the automatic segmentation of the 3D ERT model into subsurface units. Finally, resistivity models are analysed quantitatively employing a petrophysical relation of Sen et al. (1988), which predicts the dominant influence of water saturation on resistivity. This is confirmed by 2D ERT models for two monitoring periods in 2003 and 2004 with significantly different amounts of rainfall.

2. Geology

The regional geology of the Rhine valley in Northern Switzerland is characterized by sedimentary rocks formed from erosion material of the Alps. In the area of interest, the Rhine has carved a steep valley into Tertiary sandstones, in particular Saltwater Molasse from the Lower Oligocene overlain by Freshwater Molasse, a sandstone deposited in freshwater in the Upper Oligocene. Near Toessegg (Fig. 1), the north western bank rises from the present Rhine water level around 345 m above sea level (masl), with approximately 45° to a plateau of 475 masl. The south eastern bank, where the test site is located, rises more gradually (20°–30°) and the sandstone bedrock is typically covered by loose weathered or residual sands and silty sands of glacial and fluviatile origin. After several landslides had occurred on that bank in 2002, an accessible grass-covered site with an area roughly 50×20 m (Fig. 2) and located approximately 25 m above the Rhine was selected for a detailed study of the response of soil to heavy rainfall. The total height difference on the site is 25 m. At 17 m from the slope base level, a marked edge is found, dividing the slope into a lower part where the slope angle varies between 26° and 28° and an upper part with 20° inclination. According to the geological map of Hantke (1967), the transition between the Saltwater Molasse and a 2-m-thick layer of Freshwater Molasse should be found at the site. Furthermore, in the upper part of the slope, Quaternary deposits were expected as a derelict gravel pit is found even further up the slope, slightly offset from the test area. Also, thin layers of gravel and silt outcrop locally in a nearby creek. The aim of the survey was to determine the structure and thickness of these

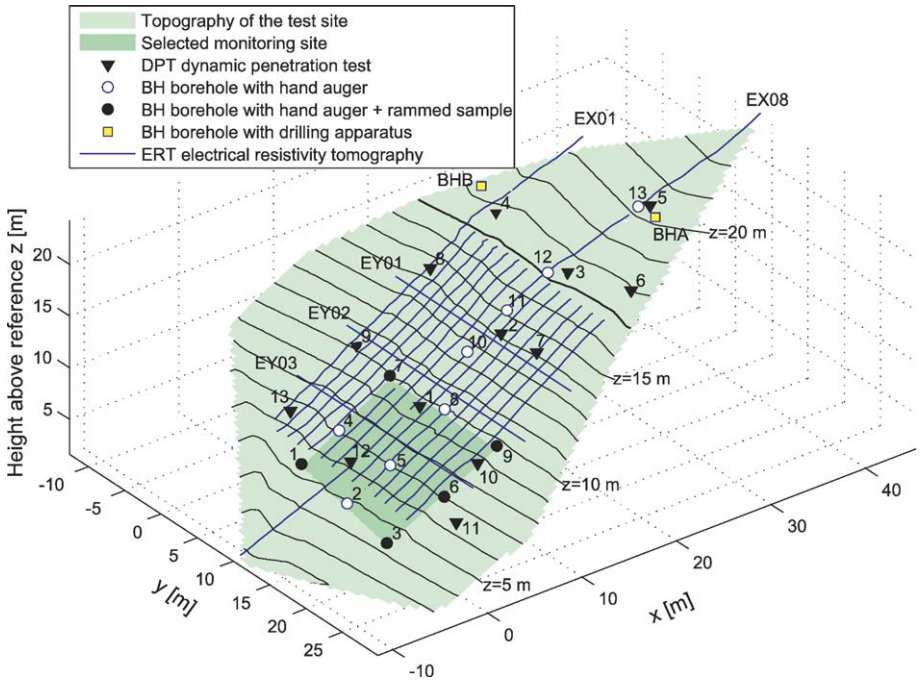

Fig. 2. Field plan of geophysical and geotechnical investigations carried out at the test site.

comparatively mobile layers above the basement, which might be most likely subject to approach failure conditions. Several smaller landslides were observed in similar ground conditions in the vicinity of the test site.

3. Methods

3.1. Electrical resistivity tomography

ERT was chosen to determine the depth to the bedrock for two reasons; firstly, it could be expected that the uncompacted sediments and the sandstone would provide a sufficient contrast in resistivity due to their differences in porosity and saturation. Secondly, the depth to the bedrock was expected at shallow depths between 1 and 2 m, so that ERT with a narrow electrode spacing would provide a high resolution. A seismic survey was ruled out due to the shallow bedrock depth and the very soft overburden that would attenuate high frequency waves needed to provide sufficient resolution. GPR measurements were carried out repeatedly with 200, 100 and 50 MHz antennae. However, high attenuation of the 200 and 100 MHz signals in the conductive silty and clayey layers found near the surface prevented sufficient depth penetration, whereas the 50 MHz antenna was unable to provide sufficient resolution of the shallow target structures at less than 2 m depths. Therefore, GPR results are not reported here.

The ERT survey in July 2003 comprised a 3D and a 2D part. The survey layout shown in Fig. 2 included resistance measurements on a grid of 17 profiles, each being 24.5 m long and comprising 50 electrodes at 0.5 m spacing. Profiles EX01 to EX14 stretched parallel to the dip of the slope, with a line spacing of 1.5 m, and 3 additional profiles EY01 to EY03 were perpendicular to the dip, and cut the EX profiles at 6, 12 and 18 profile metres. Onsite inspection of field data suggested that the subsurface resistivity varies predominantly along the slope but not perpendicular to it (2D assumption). To investigate further up and down the slope, two profiles (EX01 and EX08) were extended in length to 36 m. Additionally, EX08 was equipped with 50 electrodes with 1-m spacing to obtain a greater depth penetration to about 10 m. Using a multi-electrode system Geotom of Geolog (Germany) and conventional steel electrodes, measurements along the profiles were taken with Wenner–, Schlumberger– and Dipole–Dipole configurations of various Dipole widths of 1, 2 and 4 unit spacings. For noisy data sets, such combined data sets can significantly improve resolution and stability of the models (Friedel, 2003). Individual data sets and their resolution characteristics are discussed in Section 4.3. Each individual datum was stacked 4 times and only stacks with a standard deviation of less than 2% were accepted. The injection current density was adjusted automatically according to signal-to-noise ratio between 0.5 mA (~10% of total data), 5 mA (~80%) and 50 mA (~10%). On selected profiles, reciprocal measurements were taken (exchanging electrodes for current injection and voltage sampling) to check for reproducibility of the data. Average reciprocal errors less than 1% suggested excellent data quality and no further reciprocal data were measured. Inversion of the data was carried out with the standard Gauss–Newton codes Res2dinv/Res3dinv described by Loke and Barker (1996) and Loke (2003).

3.2. Geotechnical testing

Geotechnical testing on the site was performed after ERT reconnaissance investigation and comprised dynamic penetration tests (DPT) to detect the surface of the sandstone and boreholes including a detailed analysis of the samples with respect to grain size, density and plasticity (Fig. 2). The 13 DPT reached depths between 0.9 m and 2.3 m. Various forms of boreholes (BH) were performed in 13 additional locations with hand augers and rammed samplers. Invasions were carried out as much as possible outside the planned test area (Fig. 2). In the upper part of the slope, water was found at a depth of 1 m (after rainfall) making sampling with the hand auger impossible. Because of a smaller slope angle of about 17° a rotary drilling apparatus for boreholes BHA (to 5.8 m) and BHB (to 4.6 m) was used instead. Each soil sample taken by ramming or drilling from various depths contained more than 2 kg of material and was classified according to Swiss Standards (based on USCS). The analyses included grain size distribution by sieving (VSS, 1986) and sedimentation (VSS, 1990a), determination of the density of solids (VSS, 1990b) and plasticity analyses (VSS, 1990c). The results of these analyses use several geotechnical terms that are described in the following paragraph.

The mechanical consistency of fine-grained soil varies with water content between solid (dry), semi-solid, plastic and viscous (wet). The water contents constituting the limits between these states are called consistency limits. Two of these limits are used for the classification of soils: The liquid limit (w_L) is the water content at the limit between plastic and viscous

consistency. The plastic limit (w_P) is the water content at the limit between plastic and semi-solid consistency. The behaviour of soils under mechanical (especially shear) stress is related to the plasticity of the soil, which is related to the plasticity index (I_P), which is defined as $I_P = w_L - w_P$ (%).

In addition to obtaining the samples, the boreholes were also used to measure the groundwater level.

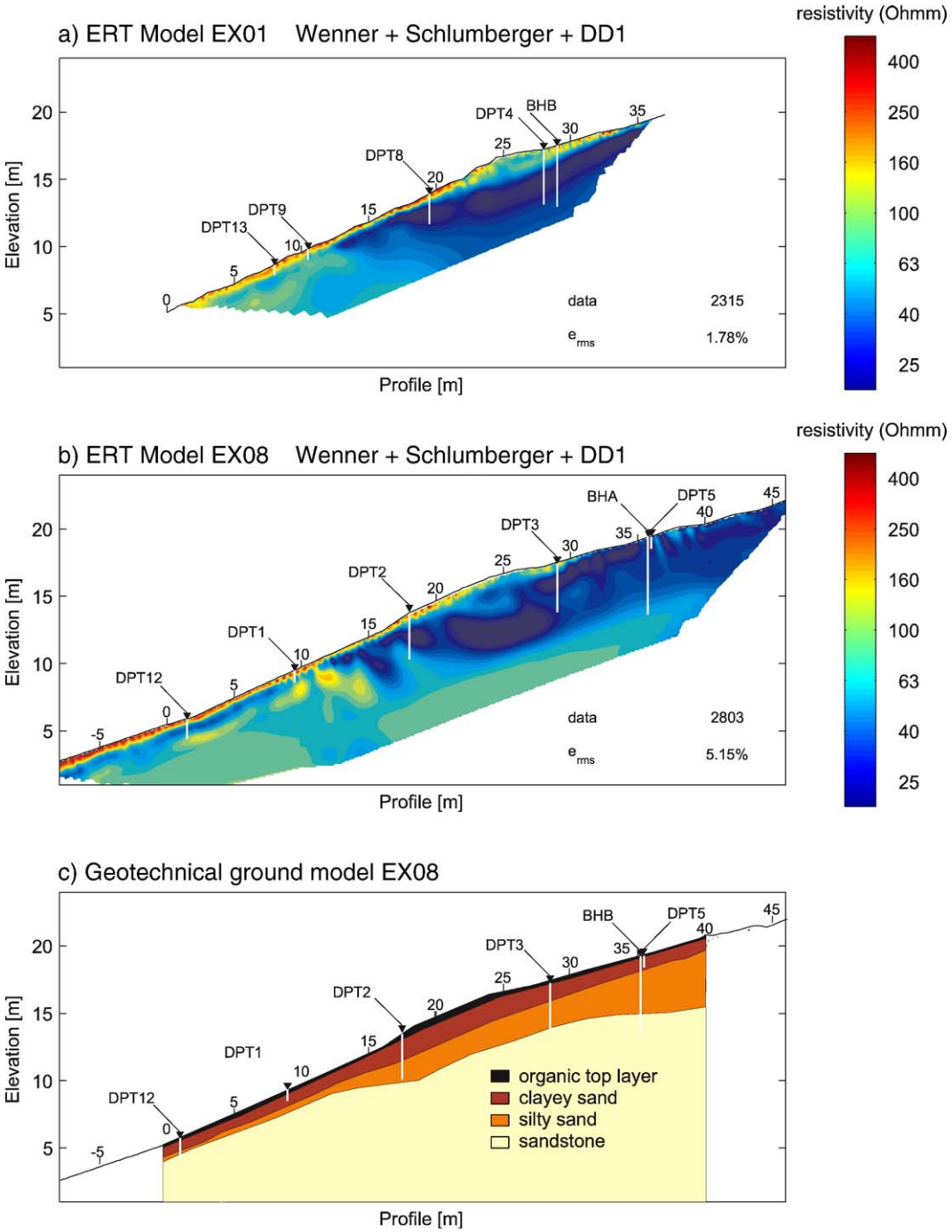

Fig. 3. 2D resistivity model based on Wenner–, Schlumberger– and Dipole–Dipole data from 2003: (a) profile EX01, (b) profile EX08, (c) 2D geotechnical model based on direct penetration tests (DPT) and borehole drillings (BH) along profile EX08. Numbers along the surface in this and all further figures show profile metres.

4. Results

4.1. 2D ERT models

Fig. 3a and b shows the results of the ERT along profiles EX01 and EX08, respectively. The resistivity model along EX01 can be divided into four units:

(i) a structure of about 100 Ω m in the lower part of the slope with a flat, nearly horizontal boundary at about 10 m above reference height,
(ii) a thin layer of up to 500 Ω m covering this unit,
(iii) a marked wedge-shaped low-resistivity anomaly (25–50 Ω m) covering the major part of the upper slope area, and
(iv) a near-surface structure with about 100 Ω m at the "hump" where the slope angle changes abruptly.

Interpretation of these resistivity structures can be attempted based on the well-known law of Archie (1942) written in terms of conductivity

$$\frac{1}{\rho} = \sigma = \frac{\Phi^m S^n}{a}\sigma_w + \sigma_c \quad (1)$$

with the resistivity ρ, the conductivity σ, the porosity Φ, the saturation S, water conductivity σ_w and the surface conductivity σ_c, in our case mainly caused by the presence of clay minerals. Even without detailed knowledge of the empirical factors m, n and a, which can only be estimated during careful laboratory tests, it is possible to attempt a geological interpretation of the ERT sections. The low-resistivity anomaly (iii) in the upper part of the slope can be caused by material high in total water content (high porosity and/or saturation), the presence of clay, or very likely a combination of those three factors. This idea is supported by the fact that water was found in BHB at 1 m depth and both BHB and DPT4 penetrated the ground for several metres before reaching the bedrock. The existence of such an extended water- and clay-bearing structure was surprising and could not be expected from the geological map produced by Hantke (1967). Downhill, the second largest unit (i) with a higher resistivity of about 100 Ω m can be attributed to the sandstone bedrock as confirmed by the shallow depths of several DPTs in that region. The sandstone lacks not only the additional clay conductivity but is supposedly also of lower porosity and permeability as it would otherwise act as an aquifer and drain the overlying saturated sediment layers.

Finally, the structural units (ii) and (iv) represent the vadose zone sediment cover on top of the sandstone- and clay-bearing sediments, respectively. A more detailed quantitative interpretation based on a more sophisticated constitutive relation accounting for clay and silt contents is presented in Section 5.

ERT section EX08 (Fig. 3b) confirms the basic structure found in EX01. Three slight modifications are found. Firstly, in the lower part of the hill, a thin low-resistivity layer (of higher water content) is present between the bedrock and the unsaturated top layer. Secondly, the upper boundary of the bedrock, nearly horizontal in EX01, appears to be somewhat rougher. Thirdly, by virtue of the longer extension of the profile allowing additional large dipole separations, it was possible to detect the approximate depth to bedrock underneath the low-resistivity anomaly. However, even with elongated dipoles, the data proved to be quite insensitive to this feature and the bedrock boundary shown in the upper part of EX08 is partly caused by an a priori model constraint derived from borehole BHA. All other models (2D and 3D) were calculated without a priori model constraints (see discussion on model quality in Section 4.3).

4.2. Geotechnical ground model

Table 1 gives an overview of all depths determined with the DPT apparatus as well as soil layers identified from borehole sampling. Good agreement has been found between the data from ERT and the DPT (Fig. 3a and b). The DPT numbers 1, 9, 10, 11, 12, and 13–all in

Table 1
Depths of boreholes and location of the layering boundaries and depth of dynamic penetration tests

DPT number	Total depth (m)	Borehole number	Depth (m) of the layer			Total depth (m)
			Humus	Clayey sand	Silty sand	
1	0.9	1	0–0.2	0.2–1.6	1.6–2.0	2.0
2	3.4	2	0–0.4	0.4–1.6	–	1.6
3	3.6	3	0–0.3	0.3–1.3	1.3–1.7	1.7
4	4.1	4	0–0.3	0.3–1.3	1.3–1.8	1.8
5	0.9	5	0–0.3	0.3–0.9	0.9–1.2	1.2
6	2.3	6	0–0.3	0.3–0.8	0.8–1.0	1.0
7	2.3	7	0–0.3	0.3–0.9	0.9–1.0	1.0
8	2.3	8	0–0.3	0.3–0.7	0.7–1.3	1.3
9	0.8	9	0–0.3	–	0.3–1.8	1.8
10	0.8	10	0–0.3	0.3–1.3	–	1.3
11	1.3	11	0–0.3	0.3–1.0	–	1.0
12	1.5	12	0–0.3	0.3–1.5	–	1.5
13	0.6	13	0–0.3	0.3–0.8	0.8–1.3	1.3
		A	0–0.2	0.2–0.5	0.5–4.6	5.8
				4.6–5.0		
		B	0–0.3	0.3–2.7	2.7–3.2	4.6
				3.2–4.6		

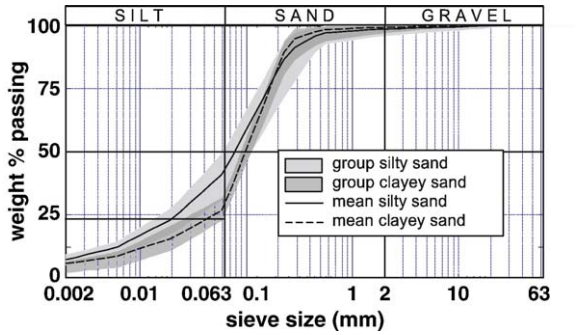

Fig. 4. Sieve curves after Swiss Standard (VSS, 1986, 1990a). Shaded areas represent the range of sieve curves for the two sand types. Lines show the average of each type.

the lower slope part–confirm depths between 0.6 and 1.5 m to the bedrock very close to the surface, as predicted by the ERT. DPT2 is also in good agreement with data derived from ERT. DPT5 on the upper slope penetrated only 0.9 m, but subsequent drilling of BHA proved a bedrock depth of 4.6 m. This shows that an intersection obtained from a DPT was not always reliable, possibly due to very high mantle friction in the silty and clayey sediments or presence of some large stones or gravel (cf. sieve curves, Fig. 4). DPTs 3, 4 and 8 also failed to reach the depth predicted by the ERT, and this is very likely to be a result of the same effect.

Soil sampling yielded additional information on the sediment layers. The sieve curves (Fig. 4) of all samples show that 50% of the soil fraction always exceeded 0.06 mm. Therefore, all samples were basically classified as sands. Depending on their fines content and plasticity analysis, the sieve curves of 21 sand samples were classified in more detail. Grains smaller than 0.06 mm in any case exceeded 20% by weight. Samples with the plasticity index (defined as liquid limit minus plastic limit) I_p of fines (<0.06 mm) <7% were classified as silty sand or silty to clayey sand. Samples with I_p of fines >7% were classified as clayey sand. The mean of each group is shown in Fig. 4 as a line, and the range of all samples are given as the shaded area. The results of the plasticity analysis are shown in Fig. 5 after the Swiss Standard (VSS, 1997), plotting the plasticity index against the liquid limit (see definitions in Section 3.2). The fines of the soil samples belong either to the groups CL-ML and ML, which indicates a silty to clayey or silty sand, or they belong to the groups CM and CL, which indicates clayey sand. The distinction between these two groups was further substantiated by a frequently observed change in soil colour at the layer boundaries; one typical example is shown in Fig. 5. Based on sieve and plasticity analyses as well as visual colour change and DPT data, the geotechnical ground model shown in Fig. 3c was derived along the profile ERT profile EX08 (Fig. 3b). Both ERT and ground model are similar to a high degree. However, sampling was able to distinguish between silty and clayey sands, which appear more homogeneous in the ERT. This contention will be discussed further in Section 5.

Measurements of the water level in the boreholes suggest that no continuous ground water level is present to the depths investigated by our survey. No water was found during drilling of BH1 to BH13. Continuous monitoring in BHA and BHB (both approximately 5 m

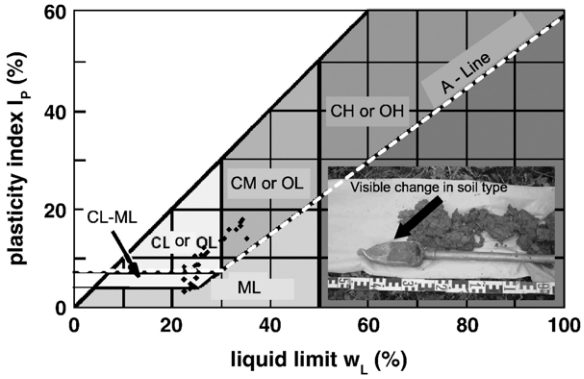

Fig. 5. Results of the plasticity analysis after Swiss Standards (VSS, 1997) based on USCS allowing a classification of the fines of the soil samples with two letters (first letter: C=clay, M=silt, O=organic; second letter: plasticity L=low, M=medium, H=high). The fines of the soil samples were found to be clay with medium to low plasticity (CM or CL), or clay/silt with low plasticity (CL-ML or ML). Based on the analysis of fines, the overall soil types could be classified into clayey sand and silty to clayey sand, which was also reflected in a marked change in soil color (photo). The A-line represents a major division in mechanical properties and is defined as $I_P=4\%$ for $w_L<25.5\%$ and $I_P=0.73\times(w_L-20)$ otherwise.

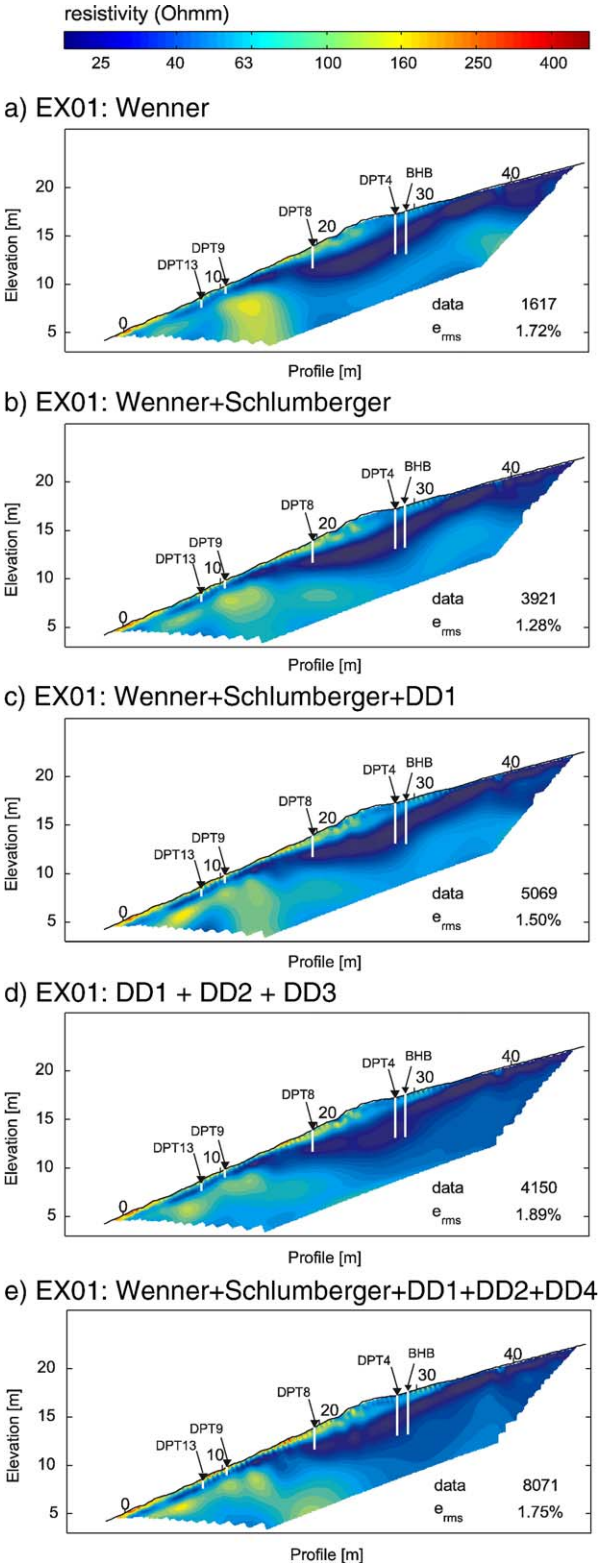

deep) shows that saturated conditions can occur after rainfall in the upper parts of the slope. However, the water level in BHB may then be at 1 m below the surface, whereas in BHA it may be at 3 m. Water may not flow in an extended aquifer but only temporarily in gravel lenses or on top of the sandstone. Where the sandstone surface is flat or even contains basins the overlying silty and clayey sediments may become more saturated as suctions are dissipated.

4.3. 2D ERT resolution analysis

Given the large amount of sampling data to verify the resistivity images, it appeared very interesting to investigate the coincidence between the geological ground model and ERT models derived from sets of different electrode configurations. The literature provides extensive discussions on the suitability of particular configurations to provide high model resolution and reliability. Recent approaches include analyses inspecting the model resolution matrix (e.g., Friedel, 2003) leading to quantitative estimates of resolvable model features, and approaches to optimize the design of geoelectrical surveys statistically (Stummer et al., 2004). In this case history, we will resort to an empirical approach (e.g., Dahlin and Zhou, 2001) to compare inversion images for several different data sets on the same profile (Fig. 6).

Fig. 6 shows the inverted images for (a) Wenner (N=1617 data), (b) Wenner+Schlumberger (N=3921), (c) Wenner+Schlumberger+Dipole–Dipole (a=0.5 m, n=1…12) (N=5069), (d) Dipole–Dipole (a=0.5 m, 1 m, 1.5 m, n=1….12) (N=4150) and (e) a sum of sets (b and d) (N=8071 data). For all data sets, the root-mean-square fitting error $e_{\mathrm{RMS}} = \sqrt{\frac{1}{N}\sum_{i=1}^{N}\left(\frac{d_i^{\mathrm{obs}} - d_i^{\mathrm{pred}}}{d_i^{\mathrm{obs}}}\right)^2}$ between observed data d^{obs} and data predicted by the model d^{pred} was very similar and ranged between 1.28% and 1.89% after five iterations. Generally, all models show the same basic features indicating high data quality and stable inversion procedure. Clearly, the image based solely on Wenner data is of the poorest resolution and cannot resolve the bedrock continuously, showing an artefact "blob" in the lower parts of the slope. Data sets (b and c) are very similar and agree best with the geological model with respect to bedrock depth. Interestingly,

Fig. 6. 2D resistivity models for selected data sets along profile EX01 measured in 2004. The image produced by Wenner data only (a) is of the poorest resolution at greater depths. The model closest to the geotechnical model is (c). Note in (d and e) how additional dipole–dipole data can change the resolution of the limestone bedrock interface and create blocky features near the surface.

adding further 3000 dipole–dipole data with larger spacings seems to bias the image towards a larger depth of bedrock and creates small scale artefacts near the surface (d and e). For that reason, and also to limit the overall data set for the monitoring campaigns, the data set 'Wenner+Schlumberger+Dipole–Dipole (unit width)' was considered to be the best compromise between resolution and measurement time and was used throughout the further studies regarding resistivity variations after rainfall and the 3D survey.

4.4. Influence of rainfall

One year after the initial resistivity survey in August 2003, the 2D ERT profile EX01 was repeated in July 2004 to detect the influence of rainfall on the degree of saturation. Both years differed significantly in precipitation. Rainfall in the months May to August amounted to [68, 41, 97, 76] mm in the comparatively dry summer of 2003, and [103, 75, 92, 88] mm in summer 2004, when approximately 30% more rain fell during the same four month period. Fig. 7 shows the resistivity images of the most interesting lower part of the slope for the 2003 survey (a) compared to 2004 (b). While the general structure of the subsurface is very similar in both years, in 2004, the low-resistivity layer between the sandstone and the superficial layer is much more distinct than in 2003. The interpretation can be made solely in terms of saturation since all other parameters can be assumed to have remained constant. It follows that after periods of extensive rainfall, major changes in water content predominantly occur in the layer on top of the sandstone. Another low-resistivity anomaly at about 15 profile metres is also more distinct in 2004, indicating that water might accumulate in individual erosion features on top of the sandstone. Meanwhile, further ERT campaigns have been conducted and will be related to rainfall TDR, suction and moisture point data in a forthcoming paper. Please note that EX01 was deliberately chosen a few metres offset from the main monitoring site (Fig. 2) in order to avoid disturbance of the ground, interference between the sensors and to aid repeatability of the experiment.

4.5. The 3D resistivity subsurface model

Fig. 3(a and b) depicting 2D ERT models along EX01 and EX08 showed a high degree of similarity in their basic structure. However, especially in the depth range interesting for the monitoring of infiltration, saturation and suction local differences occur, which are best resolved with a 3D survey. Our full 3D data set

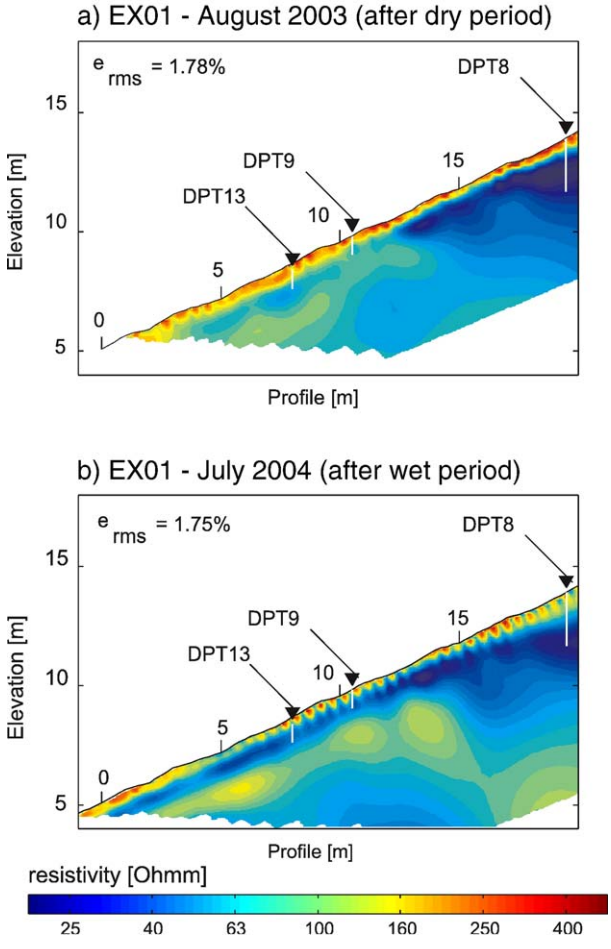

Fig. 7. Resistivity tomograms for ERT profile EX01 (a) during the dry summer 2003 and (b) after a wet period in summer 2004. The major difference occurs in the weathered layer above the sandstone.

comprised 392 Wenner data, 576 Schlumberger data, and 498 Dipole–Dipole data on each of the 17 profiles. Inversion of that data set showed an alias effect caused by the anisotropic spatial data sampling (only 3 profiles in the Y direction compared to 14 in the X direction). For that reason, only the 20,524 data from EX01 to EX14 were inverted. The model consisted of $49 \times 13 \times 11 = 7007$ model blocks with uniform cell widths of 0.5 m in x- and 1.5 m in y-directions, and cell widths in the z-direction between 0.25 m at the surface and 1 m at a depth of 6 m below the surface, reflecting the decrease of resolution with depth.

2D or 3D images inverted from geophysical fields governed by Poisson equations or diffusion equations (e.g., ERT) usually show a continuous and smooth variation of the physical parameter, whereas the geological model commonly uses discrete layer boundaries. The question about whether the continuous or

discrete model approach reflects nature more appropriately cannot be answered in general. However, given that sharp contrasts in physical properties can exist in the subsurface, geophysics should aim at inferring those structural boundaries. It is well known that multi-parameter analyses (e.g., GPR and ERT) can significantly reduce the uncertainty in geophysical interpretation (e.g., Dannowski and Yaramanci, 1999). Recently, such combined information has been used to infer structural boundaries from smooth data using stochastical cluster and fuzzy approaches (e.g., Tronicke et al., 1999; Paasche et al., submitted for publication). In our case, no GPR data could be obtained because of high attenuation in conductive soil layers. However, even in such a case, simple statistical segmentation using resistivity and spatial coordinates as descriptors may provide a useful tool to derive segmented ground models from continuous geophysical data. The efficiency of such an approach is shown in the following example, where we verify the results of a purely statistical classification of the resistivity model and the detailed geotechnical ground model derived from various methods.

We investigate the statistical distribution of the resistivity $\rho(x,y,z)$ as a function of spatial coordinates to define boundaries between soil units. Fig. 8 shows histograms of resistivity for each depth layer z_i, as estimated from the number of model cells falling into one of 60 logarithmically sized bins between 10 and 316 Ω m. Near the surface (e.g., 0.4 m depth) the distribution is unimodal and varies broadly around a resistivity value of 100 Ω m. From a depth of 2.5 m downwards, the distribution becomes clearly bimodal and varies more sharply around two maxima at 35 Ω m and 100 Ω m, separated by a minimum at 50 Ω m. Fig. 9 shows all of the histograms from Fig. 8 plotted into one diagram for the frequency of a certain value for ρ occurring at a certain depth z_i. It is possible to derive a

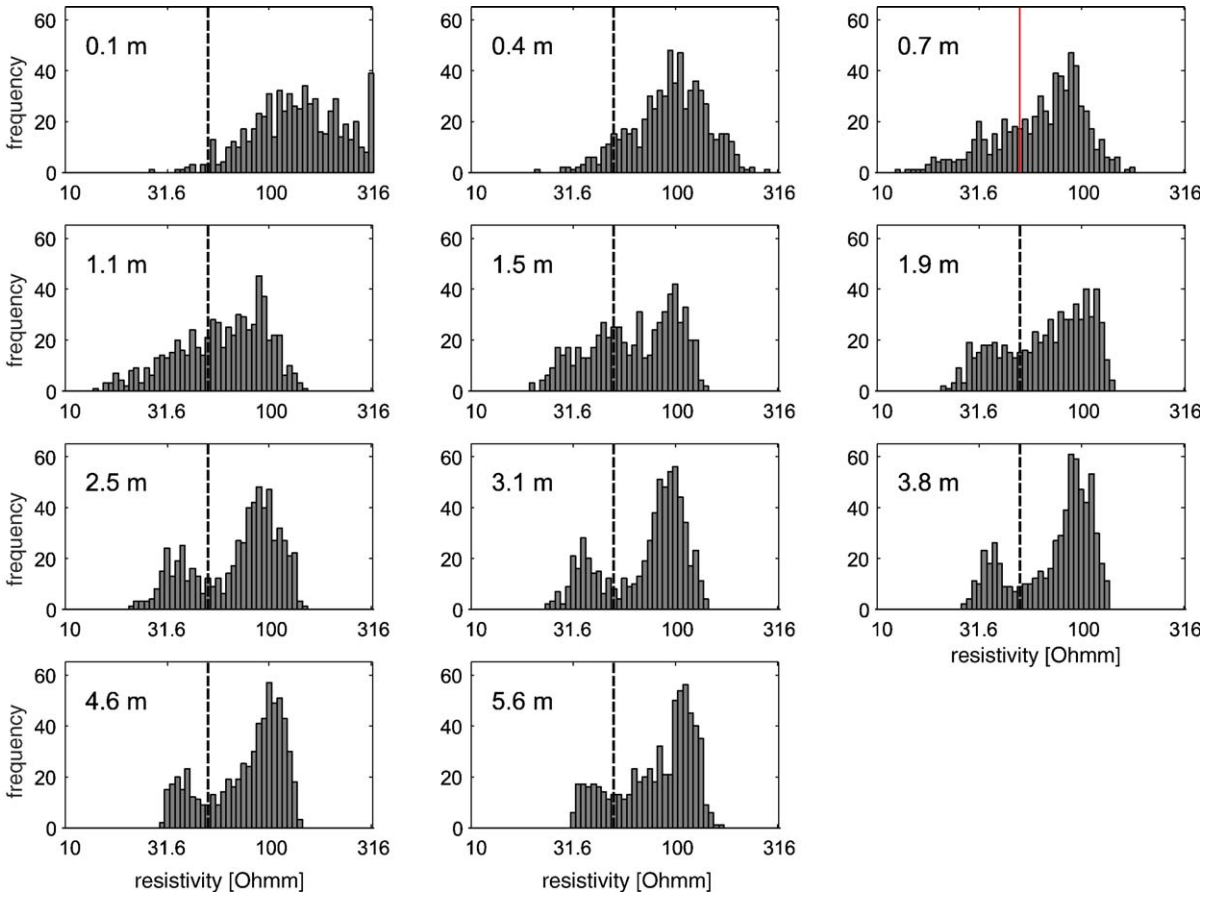

Fig. 8. Histograms showing the statistical distribution of resistivity in the 3D model as a function of depth, being unimodal near the surface and bimodal at greater depths. The strong presence of 100 Ω m material is geologically ambiguous and requires further subclassification (Fig. 9).

primary classification from this graph as follows (named after the colours in the resistivity images with which they coincide roughly, B=blue, G=green, R=red):

Class B: low resistivity $\rho<55$ Ω m, appearing at any depth, caused by silty or clayey sands with a high water saturation.

Class G: medium resistivity 55 Ω m$<\rho<$150 Ω m, which either coincides with the sandstone (low porosity) or the sands with comparatively lower saturation or clay content.

Class R: medium to high resistivity near the surface, $z_i<0.8$ m, $\rho>55$ Ω m–316 Ω m, coinciding with dry clayey or silty sands.

The ambiguity in Class G can be resolved when classifying them according to their occurrence related to the coordinate *y*. Sandstone occurs only in the

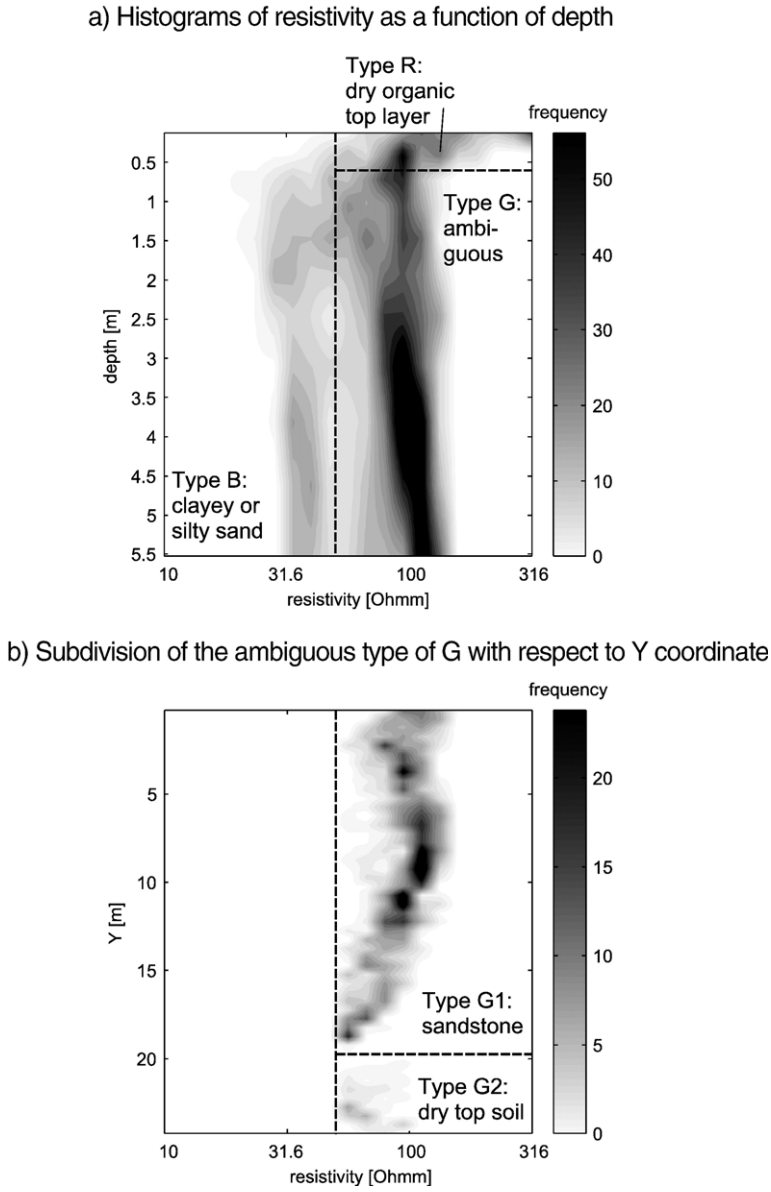

Fig. 9. (a) The histograms of Fig. 8, plotted as a frequency $h(\rho,z)$, suggest a segmentation of the subsurface into three categories. Type R: the dry organic top layer with high resistivities and shallow depths, type B: with resistivities below 55 Ω m at all depths of silty or clayey sand with a high saturation, and type G, which is ambiguous. (b) Type G can be further subdivided using the *y*-coordinate as a descriptor. This allows segmentation into two types: G1, sandstone; and G2, dry top soil.

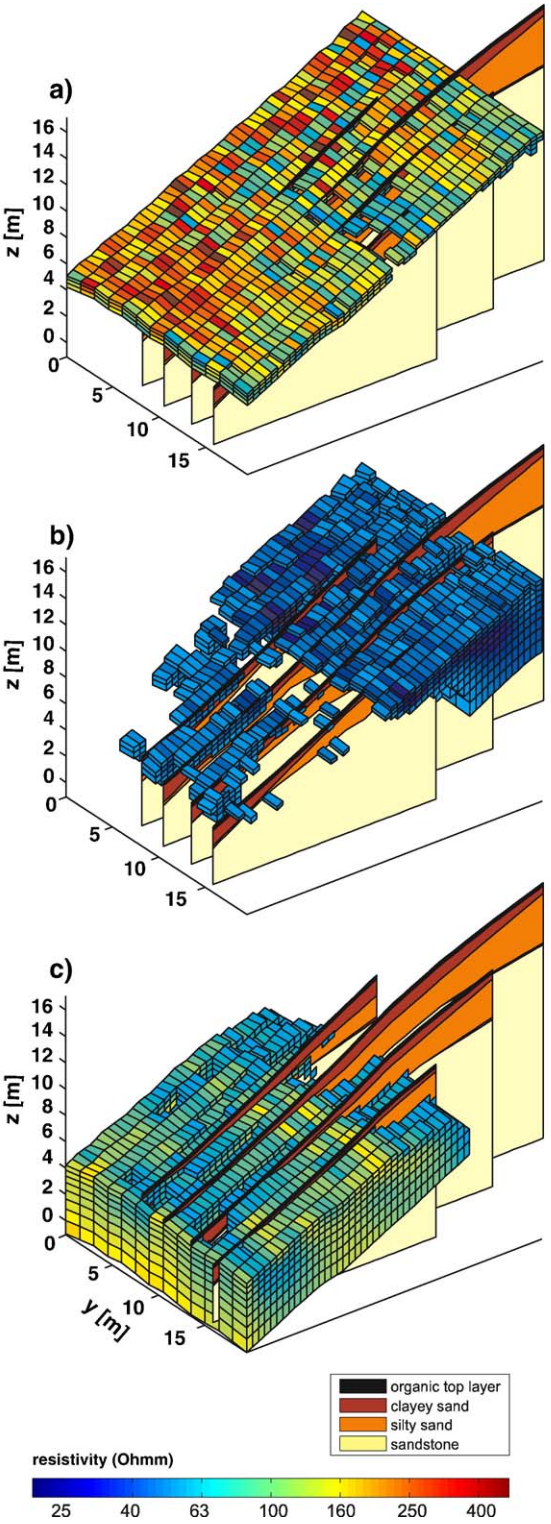

Fig. 10. Comparison of the results of the geotechnical methods (slice graphs based on drilling, sampling and dynamic penetration tests) and ERT (brick graphs) for (a) the unsaturated sandy top layer, (b) the layer of silty sand with a substantial total water content and (c) the sandstone basement.

lower part of the slope up to profile metre 19.5, forming a distinct class G1 in the frequency diagram. A second class G2 coincides with the sands with comparatively lower saturation or clay content near the surface. The suitability of this statistical classification becomes clear when comparing it to the ground model derived from drilling and sampling (Fig. 10), where an organic top layer and silty to clayey sand is found near the surface of the test site. The resistivity data tell us that soil down to about 0.8 m has a low or medium moisture content (classes R or G2, Fig. 10a). Locally, especially in the upper part of the slope, the sands have a high water content and appear as a low-resistivity zone (class B, Fig. 10b). Also, a high saturation or clay content is found locally on top of the sandstone, especially after periods of rainfall (Fig. 7b, Section 4.4). The basement of the lower slope is formed from sandstone, which is reflected in class G1 (class B, Fig. 10c). The lower part of the slope seems especially interesting with respect to slope stability, because the silty sand layers may act as narrow aquifers and may become easily saturated after rainfall, perhaps with pore pressures above the maximum hydrostatic values.

5. Discussion

During the combined interpretation of resistivity images and geotechnical model, the factors saturation, porosity and clay content were identified as crucial. To discuss these results more quantitatively and to aid further interpretation of the monitoring experiment, we use the following model of Sen et al. (1988) for the conductivity of clay bearing sandstones and their sediments:

$$\sigma = \frac{\Phi^m S^n}{a}\sigma_w\left(1+\frac{AQ_v}{\sigma_w + CQ_v}\right) + EQ_v \text{ with } Q_v = C_{ex}\rho_M\frac{1-\Phi}{\Phi} \quad (2)$$

and his choice of constants $A=3.8$ (S/m)/(mol/l), $C=0.7/Q_v$(S l)/(m mol) and $E\approx 0$ In this model, Q_v (in mol/l) isthe concentration of Na-exchange cations relative to the water saturated pore space, which depends on the cation exchange capacity C_{ex} (in mol/g) and the matrix specific density ρ_M. The dependence of the exchange capacity C_{ex} on the relative clay and silt content, P_{clay} and P_{silt} is estimated by a relationship found by Günzel (1994):

$$C_{ex} = 0.47\cdot(P_{clay} + 0.2\cdot P_{silt}). \quad (3)$$

The quantities Φ, S, P_{clay} and P_{silt} have no units in the formulae but are given as (%) in the following discussion. The influence of various parameters on that model is illustrated in Fig. 11. There, we assume an set of average parameters derived from field and literature data, and vary critical quantities along the range that can be expected in the field. In particular, we used $P_{clay}=5.5\%$, $P_{silt}=29.4\%$, $\Phi=40\%$, $S=66\%$, $\rho_M=2.65 \times 10^3$ kg/m^3 for an average silty/clayey sand, and $\sigma_w=0.067$ S/m from our field data, and the following constants for loose sands taken from Schön (1983): $a=1$, $m=2$, $n=1.3$. Based on an average model that produces a resistivity of $\rho=\sigma^{-1}=78$ Ω m, the following quantities were varied according to their range measured or expected on the site: saturation (33% … 100%), porosity (35% … 45%), clay content (1.9… 9.2%), silt content (17% … 41%), and water conductivity (0.085 … 0.115) S/m.

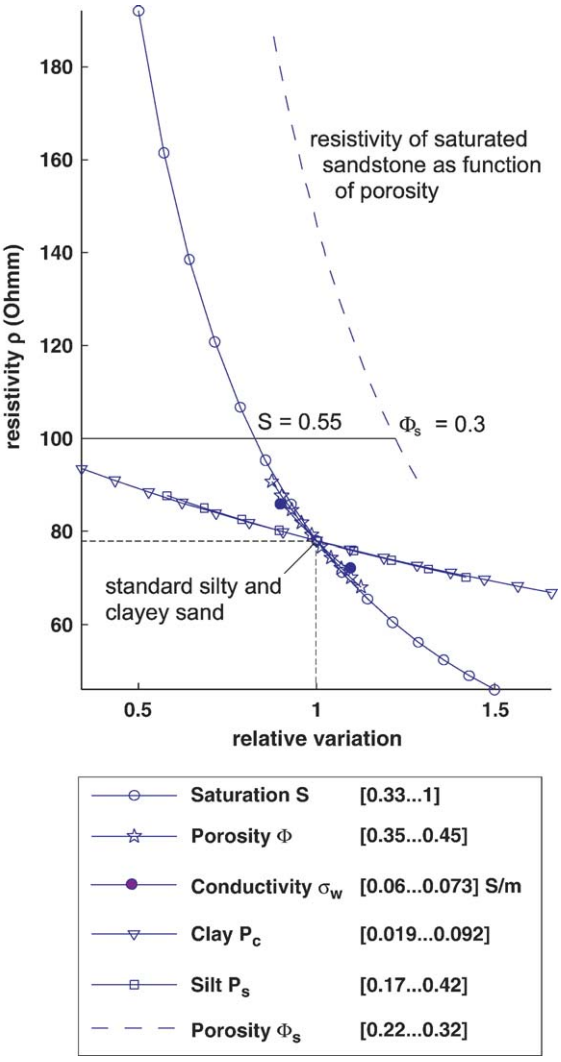

Fig. 11. Resistivity as a function of crucial soil parameters combining the models of Sen et al. (1988) and Günzel (1994). A reference model with average data, determined from our experimental data or taken from Schön (1983), produced a resistivity of 78 Ω m. Variation of individual parameters according to the range found in laboratory analysis yield the curves shown and reproduce the resistivity data measured in the field.

Fig. 11, which depicts the change of resistivity plotted vs. the relative change of each parameter, outlines the dominant influence of saturation changes, predicting a variation of the sand resistivity between 45 Ω m and 190 Ω m. The relative influence of porosity and water resistivity is almost equally as strong as each other. However, both parameters are better constrained in the field data and cause smaller total changes. Silt and clay content may vary as much as 60% from their average, but their effect on resistivity is clearly less than that of saturation. In particular, since the relative influence of both parameters is very similar, only small changes in resistivity will occur as long as the total content of silt and clay remains constant. Thus, the model explains why, in our case, clayey and silty sand layers appear as one unit in the resistivity images.

Our standard model yields 45 Ω m at full saturation and does not yet reproduce the minimum resistivity of about 35 Ω m found in the field. In order to obtain this value, we assume a higher clay and silt content. Using $P_{clay}=7\%$ and $P_{silt}=43\%$, corresponding to the maximum values determined in the sieve analysis, a resistivity of about 35 Ω m is achieved at full saturation. This illustrates the very good agreement between field and laboratory data and the petrophysical model. Finally, the model can be used to infer properties of the soil and bedrock for a resistivity of 100 Ω m, which was so commonly found at the site (Fig. 11). Such a resistivity is produced by the standard silty/clayey sand model assuming a saturation as low as 55% (class G1) but also by a saturated sandstone with a comparatively high porosity of 30% (class G2). Therefore, the model adequately explains the ambiguity in the resistivity class of 100 Ω m (class G).

6. Conclusion

The 2D and 3D ERT surveys on the test site delivered a detailed image of the near-surface conditions in generally very good agreement with drilling and sampling data. The depth to the sandstone bedrock could be determined reliably and was found to be in excellent agreement with DPT data in the lower part of the slope. In the upper part, we identified an extended formation of clayey and silty sands, which was not

expected according to geological a priori information but which was subsequently confirmed by drilling.

ERT resolution analysis proved that a combination of Wenner–, Schlumberger– and Dipole–Dipole data provided a reasonable compromise between measurement time and image resolution. It was shown that addition of further Dipole–Dipole data may not only cost disproportionately more field time but may also add unwanted bias to the model.

With the aid of a statistical classification–however crude compared to more sophisticated approaches that have been suggested for multi-parametric data–the subjectivity in interpreting the resistivity model could be decreased. The automatic classification yielded three subsurface units: bedrock, silty/clayey sands and surface layer with low partial saturation. This model was in very good agreement with the 3D geotechnical ground model.

Quantitative interpretation of the resistivity models based on a formula proposed by Sen et al. (1988) and soil parameters determined in grain size analysis could reproduce the range of resistivities found on the site very well. The model explains the ambiguity in resistivity between clayey and silty sands found on the site and predicts the dominant role of saturation. This was confirmed by two 2D ERT images taken after periods with significantly different amounts of rainfall. In the wet summer of 2004, a layer of high water saturation and permeability (silty sands) is found confined between the comparatively impermeable sandstone bedrock and a layer of clayey sands of low permeability on top. The silty sands may locally form an aquifer that can be saturated quickly after rainfall by surface infiltration or water flowing into it from higher elevations. This specific soil condition may contribute to the risk of rainfall-induced landslides in the investigated area. Consequently, the combined geophysical and geotechnical investigation suggested a particular area on the lower slope for the monitoring experiment. Given this careful choice of the site, more insight into the shallow hydraulic regime and its influence on slope stability can be expected from the ongoing measurements including tensiometers, TDR and MoisturePoints (Thielen and Springman, 2005). On the other hand, given the high resolution of ERT models reported here, a completely ERT-based 3D spatial monitoring of soil saturation (3D time-lapse tomography, e.g., Schütze et al., 2002) seems within reach. To support this approach, future analysis of soil samples should include laboratory measurements of the cation exchange capacity and the conductivity as a function of saturation.

Acknowledgements

We are most grateful to Michael Plötze for his assistance with the geological interpretation, to Marco Sperl, Rene Rohr, Markus Iten, Edi Meier, and Felix Akeret for their invaluable help in the field and the laboratory. We greatly appreciate the geophysical field equipment provided by Franz Jacobs and Alan Green. Without the kind permission of the landowner families Hiltebrandt and Gehring and tenant Mr. Fritschi, these tests would have been impossible, and we offer our grateful thanks. The project was partially supported by the Natural Hazards Network from ETH Zurich (HazNETH).

References

Archie, G.E., 1942. The electrical resistivity log as an aid in determining some reservoir characteristics. Trans. AIME 146, 54–62.

Bogoslovsky, V.A., Ogilvy, A.A., 1977. Geophysical methods for the investigation of landslides. Geophysics 42, 562–571.

Dahlin, T., Zhou, B., 2001. A numerical comparison of 2D resistivity imaging with eight electrode arrays: symposium on the application of geophysics to engineering and environmental problems. Environ. Eng. Geophys. 977–983.

Dannowski, G., Yaramanci, U., 1999. Estimation of water content and porosity using combined radar and geoelectrical measurements. Eur. J. Environ. Eng. Geophys. 4, 71–85.

Fischer, C., López, J., Springman, S.M., 2003. Remediation of an eroded steep slope in weathered sandstone after a major rainstorm. International Conference on Landslides, Hong Kong, 8–10 Dec.

Frappa, M., Lebourg, T., 2001. Mesures geophysiques pour l'analyse des glissements de terrain, translated title: geophysical survey for landslide analysis. Rev. Fr. Géotech. 95–96, 33–40 (in French).

Fredlund, D.G, Rahardjo, H., 1993. Soil Mechanics for Unsaturated Soils. John Wiley & Sons, Inc.

Friedel, S., 2003. Resolution, stability and efficiency of resistivity tomography estimated from a generalized inverse approach. Geophys. J. Int. 153, 305–316.

Godio, A., Bottino, G., 2001. Electrical and electromagnetic investigation for landslide characterisation. Phys. Chem. Earth (C) 26, 705–710.

Günzel, F., 1994. Geoelektrische Untersuchung von Grundwasserkontaminationen unter Berücksichtigung des Einflusses von Ton- und Wassergehalt auf die elektrische Leitfähigkeit des Untergrundes. Phd thesis, Ludwig-Maximilians-Universität München (in German).

Hack, R., 2000. Geophysics for slope stability. Surv. Geophys. 1 (4), 423–448.

Hantke, R., 1967. Geologische Karte des Kantons Zürich und seiner Nachbargebiete. Kommissionsverlag Leemann, Zürich.

Lapenna, V., Lorenzo, P., Perrone, A., Piscitelli, S., Sdao, F., Rizzo, E., 2003. High-resolution geoelectrical tomographies in the study of the Giarrossa landslide (southern Italy). Bull. Eng. Geol. Environ. 62, 259–268.

Loke, M.H., 2003. RES2DINV Rapid 2-D Resistivity and IP inversion using the least squares method. Manual, Geotomo Software, Penang, Malaysia.

Loke, M.H., Barker, R.D., 1996. Rapid least-squares inversion of apparent resistivity pseudosections by a Quasi-Newton method. Geophys. Prospect. 44, 131–152.

McCann, D.M., Forster, A., 1990. Reconnaissance geophysical methods in landslide investigations. Eng. Geol. 29, 59–78.

Paasche, H., Tronicke, J., Holliger, K., Green, A., submitted for publication. Integration of diverse physical-property models: Subsurface zonation and petrophysical parameter estimation based on fuzzy c-means cluster analyses. Geophysics.

Schmutz, M., Albouy, Y., Gurin, R., Maquaire, O., Vassal, J., Schott, J.-J., Desclotres, M., 2000. Joint Electrical and Time Domain Electromagnetism (TDEM) data inversion applied to the super sauze earthflow (France). Surv. Geophys. 21 (4), 371–390.

Sen, P.N., Godde, P.A., Sibbit, A., 1988. Electrical conduction in clay bearing sandstones at low and high salinities. J. Appl. Phys. 63, 4832–4840.

Schön, J., 1983. Petrophysik. Physikalische Eigenschaften von Gesteinen und Mineralen. Akademie-Verlag, Berlin.

Schütze, C., Friedel, S., Jacobs, F., 2002. Detection of three-dimensional transport processes in porous acquifers using geoelectrical process quotient tomography. Eur. J. Environ. Eng. Geophys. 7, 3–19.

Springman, S., Jommi, C., Teysseire, P., 2003. Instabilities on moraine slopes induced by loss of suction: a case history. Geotechnique 53 (1), 3–10.

Stummer, P., Maurer, H., Green, A., 2004. Experimental design: electrical resistivity data sets that provide optimum subsurface information. Geophysics 69, 120–139.

Suzuki, K., Higashi, S., 2001. Groundwater flow after heavy rain in landslide-slope area from 2-D inversion of resistivity monitoring data. Geophysics 66 (3), 733–743.

Thielen, A., Springman, S.M., 2005. First results of a monitoring experiment for the analysis of rainfall induced landslides. In: Tarantino, A., Romero, E., Cui, Y.J. (Eds.), Advanced Experimental Unsaturated Soil Mechanics—Proceedings of an International Symposium, Trento, Italy, 27–29 June 2005–EXPERUS. Taylor and Francis, London.

Thielen, A., Friedel, S., Plötze, M., Springman, S.M., 2005. Combined approach for site investigation in terms of the analysis of rainfall induced landslides, 16th ICSMGE Sept. 12-16, Osaka, ISSMGE, 2591–2594.

Tronicke, J., Blindow, N., Gross, R., Lange, M.A., 1999. Joint application of surface electrical resistivity–and GPR–measurements for groundwater exploration on the island of Spiekeroog—northern Germany. J. Hydrol. 223, 44–53.

VSS, 1986. Mineralische Baustoffe und Lockergesteine–Siebanalyse. Schweizer Norm SN 670810c.

VSS, 1990a. Mineralische Baustoffe, Schlämmanalyse nach der Aräometermethode. Schweizer Norm SN 670816a.

VSS, 1990b. Versuche: Dichte des Bodens. Schweizer Norm SN 670335a.

VSS, 1990c. Konsistenzgrenzen. Schweizer Norm SN 670345a.

VSS, 1997. Identifikation der Lockergesteine-Labormethode mit Klassifikation nach USCS. Schweizer Norm SN 670 008a.